Chinese Chemical Letters 34 (2023) 107524

Contents lists available at ScienceDirect

Chinese Chemical Letters

journal homepage: www.elsevier.com/locate/cclet

# Highly exposed $NiFeO_x$ nanoclusters supported on boron doped carbon nanotubes for electrocatalytic oxygen evolution reaction

Liyang Lv, Bing Tang, Qianqian Ji, Na Li, Yao Wang, Sihua Feng, Hengli Duan, Chao Wang, Hao Tan*, Wensheng Yan*

*National Synchrotron Radiation Laboratory, University of Science and Technology of China, Hefei 230026, China*

ARTICLE INFO

*Article history:*
Received 4 January 2022
Revised 14 March 2022
Accepted 12 May 2022
Available online 16 May 2022

*Keywords:*
Highly exposed
Electrocatalyst
*In-situ* XAFS
B-dope CNTs
Ni-Fe oxides

ABSTRACT

The development of efficient and cost-effective electrocatalysts for oxygen evolution reaction (OER) is crucial for the overall water splitting. Herein, we prepared a highly exposed $NiFeO_x$ ultra-small nanoclusters supported on boron-doped carbon nonotubes catalyst, which achieves a 10 mA/cm$^2$ anodic current density at a low overpotential of 213 mV and the Tafel slope of 52 mV/dec in 1.0 mol/L KOH, superior to the pristine $NiFeO_x$-CNTs and other state-of-the-art OER catalysts in alkaline media. A combination study (XPS, sXAS and XAFS) verifies that the local atomic structure of Ni and Fe atoms in the nanoclusters are similar to NiO and $Fe_2O_3$, respectively, and the B atoms which are doped into the crystal lattice of CNTs leads to the optimization of Ni 3d $e_g$ orbitals. Furthermore, *in-situ* X-ray absorption spectroscopies reveal that the high valence state of Ni atoms are served as the real active sites. This work highlights that the precise control of highly exposed multicomponent nanocluster catalysts paves a new way for designing highly efficient catalysts at the atomic scale.

© 2023 Published by Elsevier B.V. on behalf of Chinese Chemical Society and Institute of Materia Medica, Chinese Academy of Medical Sciences.

Hydrogen is deemed to one of the most potential clean energies with the highest mass-specific energy density in the 21st century [1]. From a renewable and inoffensive perspective, electrochemical water splitting represents a carbon-free and environment-friendly strategy for hydrogen production [2–4]. However, the sluggish kinetics of the oxygen evolution reaction (OER) in the cathode largely limits energy conversion efficiency in comparison to hydrogen evolution reaction (HER) [5–7]. The state-of-the-art catalysts such as $RuO_2$ and $IrO_2$ have exhibited desirable OER activity [8], however, the high cost and low reserves of these precious metals make it not appropriate for practical large-scale application [9]. It is thus imperative to develop highly efficient and earth-abundant OER electrocatalysts. First-row (3d) transition metals-based components, including single atom catalysts [10,11], transition-metal (Ni, Fe, Co) hydroxides [12–14] and metal-organic frameworks [15], have emerged as promising candidates for OER catalysts. Among them, Ni-Fe oxide catalysts have been attracted much attention due to their excellent electrocatalytic performances [16,17]. However, the poor electronic conductivity and the insufficient surface with exposed active sites of Ni-Fe oxide hinder their practical application. Therefore, it is still highly desired to develop the Ni-Fe oxide catalysts with excellent OER performance and low cost.

Recently, Ding Ma *et al.* have reported a new type of catalyst named fully exposed cluster catalyst (FECC) with high surface area [18]. The dispersion of active metal atoms is much higher than nanoparticle catalyst, which makes it possible for FECC to maintain a highly atomic utilization efficiency. Geometrically, the ultra-small clusters also expose more low-coordination sites that considerably change the breaking and forming of chemical bond during the reaction. Simultaneously, compared with single atom catalysts that present the highly discrete metal centers, the FECC could offer multiple metal atoms at the same surface site, which is critically significant in the adsorption and transformation of diverse reactants or intermediates. The rich surface-site diversity endows FECC with excellent reactivity toward certain reaction paths [19]. For instance, Yang *et al.* successfully synthesized subnanometer iron oxide clusters, which exhibits much higher catalytic activity for the Fischer–Tropsch synthesis reaction on account of their higher fraction of exposed surfaces [20]. Inspired by FECC, highly exposed Ni-Fe oxide nanocluster will be a promising catalyst to achieve exceptional OER performance. Considering the fact that the size and performance of catalysts are strongly relevant to their interactions with the supports, thus, one of the important issues for the formation of highly exposed nanocluster catalysts is to choose a suitable support which deliberately tunes the catalyst-support interactions, avoiding the unintentional formation of nanoparticles or single atoms. Carbon-based nanomaterials, such as carbon nanotubes

* Corresponding authors.
*E-mail addresses:* talkhao@ustc.edu.cn (H. Tan), ywsh2000@ustc.edu.cn (W. Yan).

https://doi.org/10.1016/j.cclet.2022.05.038
1001-8417/© 2023 Published by Elsevier B.V. on behalf of Chinese Chemical Society and Institute of Materia Medica, Chinese Academy of Medical Sciences.

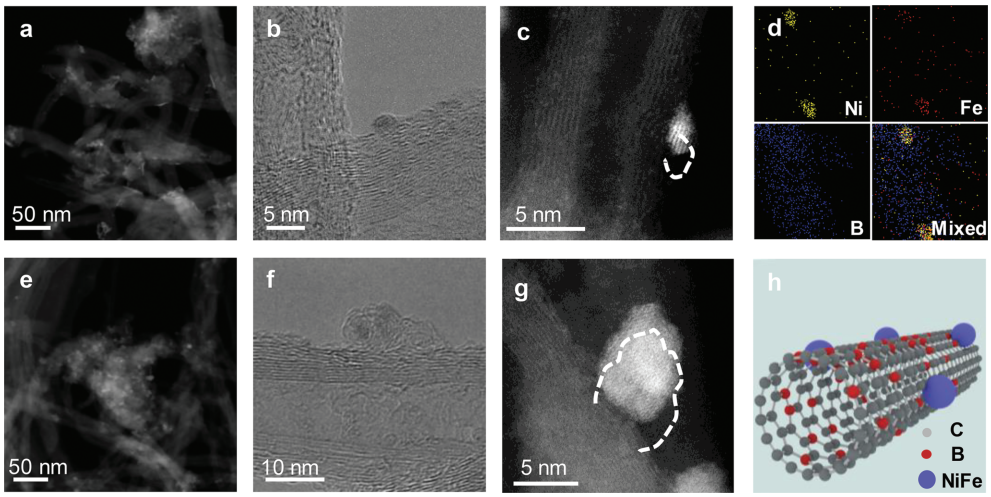


**Fig. 1.** TEM images of $NiFeO_x$-B@CNTs with low (a) and high (b) magnification. (c) HAADF-STEM image of the nanocluster of $NiFeO_x$-B@CNTs. (d) Elemental mappings image of $NiFeO_x$-B@CNTs. TEM images of $NiFeO_x$-CNTs with low (e) and high (f) magnification. (g) HAADF-STEM image of the nanocluster of $NiFeO_x$-CNTs. (h) Optimized structure of $NiFeO_x$ clusters embedded into B-doped CNTs from side view.

(CNTs), graphene, and functionalized carbon are identified as appropriate support materials because of their high surface area and conductivity [21]. However, the weak interactions between metal and carbon materials spark a flurry of the Ostwald ripening effects which means the migration and aggregation of metal atoms [22]. Alternatively, substitution of carbon atoms by heteroatoms in carbon materials is an advisable method to regulate the interactions between metal and substrates. Whereas, according to previous reports, highly electronegative heteroatoms (*e.g.*, N and P) are introduced to anchor metal atoms, leading to the formation of single-atom catalysts [23,24]. Based on this, it is essential to find a heteroatom-doped carbon matrix that interacts with metal neither too strong nor too weak for the synthesis of nanoclusters. Due to an appropriate interaction between the metal and boron (B) atoms, B-doped CNTs might be a promising candidate. In addition, doping B in CNTs induces a partial positive charge and forming electron deficiency for "p-type doping", promoting the electron transfer [25]. Therefore, B-doped CNTs is a suitable candidate for the support material. Nevertheless, few studies have built bridges between B-doped CNTs and Ni-Fe oxide catalysts and find out the modification effects of B atoms in these catalysts.

In this work, targeting the fact that the low atomic utilization efficiency and electrical conductivity are the major limiting factors of Ni-Fe oxide catalysts activity. We prepared a highly exposed $NiFeO_x$ nanoclusters supported on B-doped CNTs catalyst, which exhibits superior performance for OER, with an overpotential as low as 213 mV at 10 $mA/cm^2$ and a Tafel slope of 52 mV/dec, far better than the commercial $RuO_2$ catalyst with the overpotential of 302 mV. The HAADF-STEM verifies that the size of $FeNiO_x$ compounds dramatically reduces to highly exposed nanoclusters after doping B atoms. A combination study (XAFS, XANES, XPS and sXAS) reveals the local atomic structure of Ni and Fe atoms in the nanoclusters are similar to NiO and $Fe_2O_3$ and doped B atoms change the 3d $e_g$ orbital occupation of Ni element. Furthermore, by using the *in-situ* XAFS, we directly observe that the high-state Ni atoms act as the real active sites. The enhanced activity of $NiFeO_x$-B@CNTs could be ascribed to the unique B doping, which brings about multiple beneficial factors for OER catalysis: highly exposed surface active sites, optimization of the Ni 3d $e_g$ orbital and increased electrical conductivity.

The $NiFeO_x$ clusters supposed on CNTs were synthesized through a facile two-step strategy. More details are described in Supporting information. In order to investigate the micromorphology of $NiFeO_x$-B@CNTs and $NiFeO_x$-CNTs, transmission electron microscopy (TEM), high-angle annular dark-field scanning transmission electron microscopy (HAADF-STEM) and Energy-dispersive spectroscopy (EDS) mapping were performed. Figs. 1a and b show TEM images of $NiFeO_x$-B@CNTs. It is obvious that abundant island-like nanoclusters were grown over the surface of B-doped CNTs. The HAADF-STEM (Fig. 1c) shows the sizes of the nanoclusters are ~2 nm with highly exposed surface (the white line). Additionally, EDS mapping (Fig. 1d) reveals uniform spatial distribution of B in CNTs, in contrast, Ni, Fe agglomerate together to form the nanoclusters on the surface of $NiFeO_x$-B@CNTs. However, for the sample without B-doped, the sizes of the nanoclusters are ~10 nm (Figs. 1e-g). And the charts of particle size distribution (Fig. S1 in Supporting information) manifest that the size of the clusters in $NiFeO_x$-B@CNTs is wildly smaller than that of $NiFeO_x$-CNTs. More importantly, Fig. S1 shows the relationship of the size dependence on the doped B content, inferring the doped B in the CNTs play a critical role in reducing the size of nanoclusters. Taking together, we successfully constructed the ultra-small and highly exposed NiFe-based nanoclusters on the B@CNTs (Fig. 1h).

The determination of local atomic structure of NiFe-based compound is extremely significant to explore the real active species. Whereas conventional characterized techniques such as TEM (Fig. S2 in Supporting information) or XRD (Fig. S3 in Supporting information) are difficult to give the exactly structural information of the ultra-small nanoclusters. Therefore, we used X-ray absorption fine structure (XAFS), which is high sensitivity to local chemical environment of the materials [20], to study the phase composition and microstructure of the NiFe-based clusters. From the Ni K-edge XANES spectra (Fig. 2a), both $NiFeO_x$-B@CNTs and $NiFeO_x$-CNTs are observed a strong signal at 8350 eV, which are similar to the commercial NiO but different from that of Ni foil. This observation is validated by the EXAFS as well. As shown in Fig. 2b, two strong peaks of $NiFeO_x$-B@CNTs and $NiFeO_x$-CNTs located at 1.6 and 2.6 Å which are assigned to Ni–O and Ni–Ni scattering feature, respectively. The positions of these two peaks are in alignment with those of the N–O and Ni–Ni scattering paths of NiO [26], suggesting the local structure of Ni atoms in the nanoclusters is similar to NiO. Similar approach was also used to analyze the Fe K-edge XANES spectra (Fig. 2c) and the EXAFS spectra (Fig. 2d), and

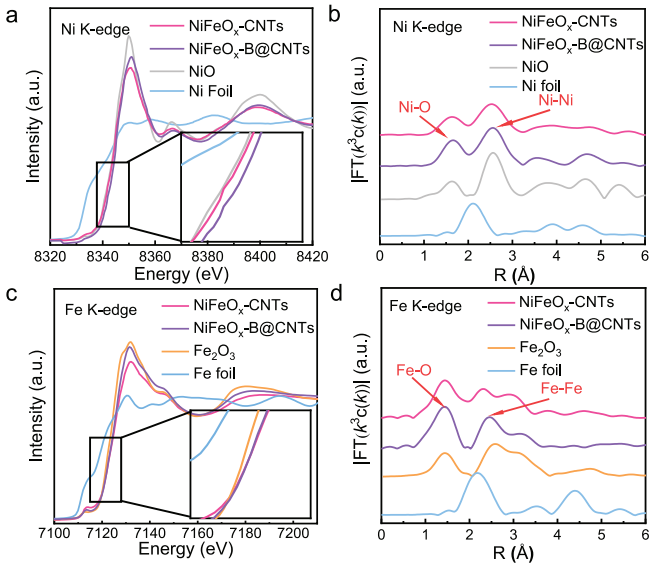


**Fig. 2.** (a) Ni K-edge XANES spectra of $NiFeO_x$-CNTs, $NiFeO_x$-B@CNTs, NiO and Ni foil. (b) $k^3$-weighted FT spectra in R-space at the Ni K edge. (c) Fe K-edge XANES spectra $NiFeO_x$-CNTs, $NiFeO_x$-B@CNTs, $Fe_2O_3$ and Fe foil. (d) $k^3$-weighted FT spectra in R-space at the Fe K-edge.

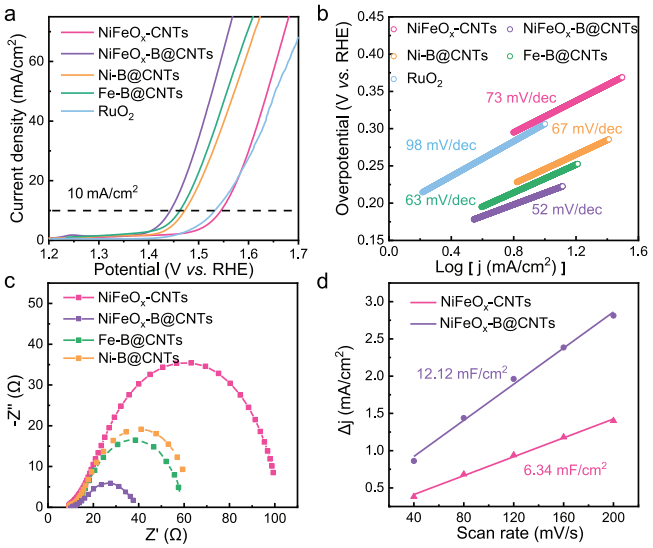


**Fig. 3.** (a) LSV curves of $NiFeO_x$-CNTs, $NiFeO_x$-B@CNTs, Ni-B@CNTs, Fe-B@CNTs and $RuO_2$ at a scan rate of 10 mV/s. (b) Corresponding Tafel plots. (c) Nyquist plots of $NiFeO_x$-B@CNTs, $NiFeO_x$-CNTs, Ni-B@CNTs, Fe-B@CNTs and $RuO_2$ at 240 mV overpotential in 1 mol/L KOH. (d) The difference in current density between the anodic and cathodic sweeps *versus* scan rate of $NiFeO_x$-CNTs and $NiFeO_x$-B@CNTs.

the Fe characteristic peaks of $NiFeO_x$-B@CNTs and $NiFeO_x$-CNTs are similar to the standard sample of $Fe_2O_3$. These results demonstrate that the details of local atomic structure of Ni and Fe atoms are similar to NiO and $Fe_2O_3$. What is more, as shown in Fig. 2a and insert, the position of the absorption edge slightly moved toward the higher energy side with the boron doping, implying that the unoccupied 3d hybrid orbitals the Ni atoms is increased. In contrast, the position of the adsorption edge of the Fe K-edge XANES remain unchanged. Those are in agreement with the results of XPS and soft XAS spectra that will be discussed later.

The electrocatalytic OER activities of the catalysts were evaluated by a standard three-electrode system in 1.0 mol/L KOH electrolyte. The HgO electrode and platinum net were used as reference electrode and counter electrode, respectively. The polarization curves of as-prepared catalysts were obtained by the linear sweep voltammetry (LSV) at a scan rate of 10 mV/s, without *iR*-correction. As shown in Fig. 3a, the LSV curves illustrate that the $NiFeO_x$-B@CNTs exhibits substantially improved OER performance compared to that of the $NiFeO_x$-CNTs. The overpotential of $NiFeO_x$-B@CNTs was 213 mV, which is much lower than the other samples (242 mV for Ni-B@CNTs, 232 mV for Fe-B@CNTs, 314 mV for $NiFeO_x$-CNTs and 302 mV for commercial $RuO_2$ which is consistent with previous work [27]), indicating that B atoms play a vital role in improving the intrinsic catalytic activities. Fig. 3b compares the kinetics of the intrinsic activities by Tafel plots acquired from corresponding polarization curves, and manifests the Tafel slope of $NiFeO_x$-B@CNTs is only 52 mV/dec, considerably

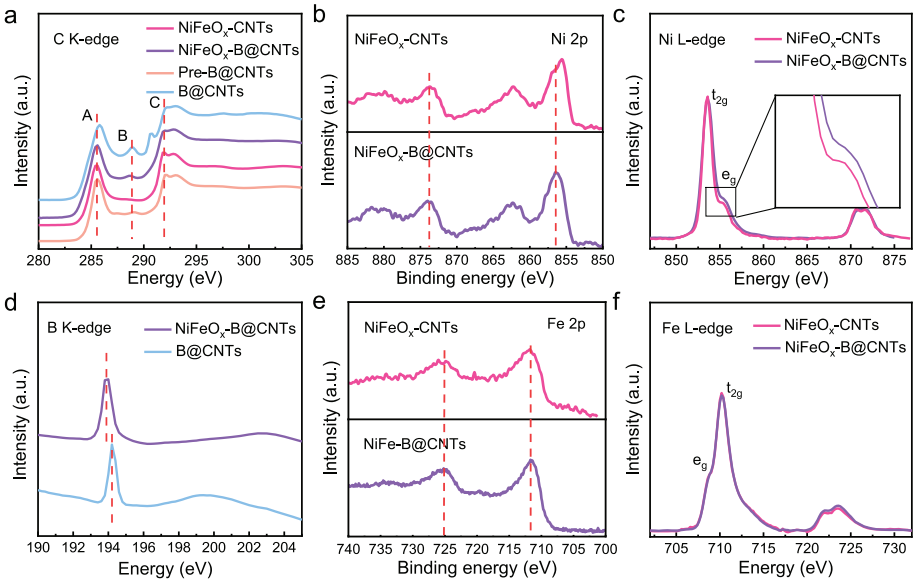


**Fig. 4.** (a) C K-edge soft XAS spectra of $NiFeO_x$-CNTs, $NiFeO_x$-B@CNTs, Pre-B@CNTs and B@CNTs. (b) Ni 2p XPS of the $NiFeO_x$-CNTs and $NiFeO_x$-B@CNTs. (c) Ni L-edge soft XAS spectra of the $NiFeO_x$-CNTs and $NiFeO_x$-B@CNTs. (d) B K-edge soft XAS spectra of the $NiFeO_x$-B@CNTs and B@CNTs. (e) Fe 2p XPS of the $NiFeO_x$-CNTs and $NiFeO_x$-B@CNTs. (f) Fe L-edge soft XAS spectra of the $NiFeO_x$-CNTs and $NiFeO_x$-B@CNTs.

lower than those Fe-B@CNTs (63 mV/dec), Ni-B@CNTs (67 mV/dec), $NiFeO_x$-CNTs (73 mV/dec) and $RuO_2$ (98 mV/dec). This suggests the rate-determination step has been changed after the B doping. To further understand the electrical exchange between the electrolyte and electrode, we measured the electrochemical impedance spectroscopy (EIS) of all electrocatalysts (Fig. 3c). The total charge-transfer resistances ($R_{ct}$) of Fe-B@CNTs, Ni-B@CNTs and $NiFeO_x$-CNTs are 49.2, 52.7 and 91.2 Ω, respectively, while the $R_{ct}$ of $NiFeO_x$-B@CNTs is as small as 28.3 Ω at the 240 mV overpotential. A direct comparison between $NiFeO_x$-B@CNTs and others clearly illustrates that the $NiFeO_x$-B@CNTs possesses a fast charge transfer process and a low kinetic impedance. Additionally, we evaluate the electrochemical surface areas (ECSA) of $NiFeO_x$-B@CNTs and $NiFeO_x$-CNTs by double-layer capacitance ($C_{dl}$). As shown in Fig. 3d and Fig. S4 (Supporting information), the $C_{dl}$ of $NiFeO_x$-B@CNTs is 12.12 mF/cm$^2$, which is 1.9 times higher than $NiFeO_x$-CNTs (6.34 mF/cm$^2$), inferring that the $NiFeO_x$-B@CNTs has larger active surface areas. As a momentous indicator for practical application, the stability the $NiFeO_x$-B@CNTs is one of the most noteworthy features. The long-term chronoamperometric experiment was done to assess the stability of catalyst (Fig. S5 in Supporting information). At 1.44 V *versus* RHE, the curve of $NiFeO_x$-B@CNTs exhibits litter deterioration during the 20 h tests, highlighting a superior durability and excellent stability. To sum up, based on the above electrochemical experimental results, we infer that $NiFeO_x$-B@CNTs underwent an activation process boosted by doped B atoms that contributes to its remarkable OER performance.

To unravel the origin of the distinguished OER performance of the $NiFeO_x$-B@CNTs from the electronic level, we used the X-ray photoelectron spectroscopy (XPS) and *ex-situ* soft XAS to gain an insight into the electron interaction between B doped CNTs and $NiFeO_x$ nanoclusters. The C K-edge soft XAS spectra of $NiFeO_x$-CNTs and $NiFeO_x$-B@CNTs are shown in Fig. 4a, and the B@CNTs and CNT are also given for comparison. The peak A at 285.6 eV and peak C at 292.1 eV can be assigned to the $\pi^*$ excitation the $\sigma^*$ excitation of C–C bonds, respectively [28,29]. These two peaks are similar in all samples, inferring that the carbon support was still graphitized after doped by B atoms. Whereas, a new peak located at 288.9 eV, which may assign to the excitation of C–B bonds [30], is observed in $NiFeO_x$-B@CNTs and B@CNTs, implying that the B atoms have been doped into the crystal lattice of CNTs. The XPS of B 1s spectrum for the $NiFeO_x$-B@CNTs (Fig. S6 in Supporting information) is deconvoluted into three distinct characteristic peaks, and the peaks located at 187.6 eV, 189.5 eV and 192.4 eV are corresponding to the $B_4C$, $BC_3$ and $BCO_2$ structures, respectively, which is in agreement with reported results [30–32]. This is further supported by the XPS of C 1s spectra (Fig. S7 in Supporting information), where a difference at 283.7 eV, which assigned to B-C bond, was observed in the $NiFeO_x$-B@CNTs. For $NiFeO_x$-CNTs, the Ni 2p spectrum (Fig. 4b) exhibits two broad peaks at 873.9 (Ni $2p_{1/2}$) and 855.6 eV (Ni $2p_{3/2}$) along with two shakeup satellites at 878.4 and 860.1 eV. Those are characteristic peaks for the $Ni^{2+}$ oxidation state [33,34]. After boride treatment, the peak centered at 855.6 eV shifts to a higher energy, suggesting there are some electrons transferring out from the Ni atoms. This scenario is also confirmed by the Ni $L_{2,3}$-edge spectra (Fig. 4c and insert), which is originated from the dipole transitions from $2p_{1/2}$ and $2p_{3/2}$ core levels to the unoccupied 3d hybrid orbitals, and the peaks at 853.6 eV and 855.2 eV are assigned to Ni 3d $t_{2g}$ and 3d $e_g$ sub-bands [35]. Noteworthy that the intensity of Ni 3d $e_g$ peak is intensified after boronation, implying that the 3d $e_g$ electron occupation of the Ni atoms is decreased. In contrast, without any change was observed in the Fe 2p XPS spectra (Fig. 4e) and Fe $L_{2,3}$-edge XANES spectra (Fig. 4f). More importantly, from Fig. 4d, it can be seen that the B K-edge of B@CNTs shift from 194.2 eV to 193.8 eV, indicating that B atoms accept the electron from $NiFeO_x$ nanoclusters. These results indicate that the electrons transfer from Ni 3d $e_g$ to the B 2p. As a consequence, the optimized electronic structure of Ni could effectively improve the OER performance of $NiFeO_x$ nanoclusters.

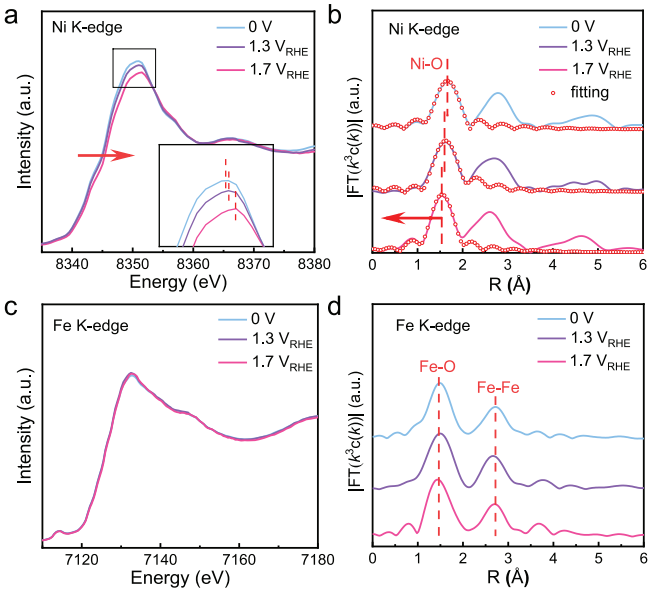


**Fig. 5.** (a) *In-situ* Ni K-edge XANES spectra of $NiFeO_x$-B@CNTs. (b) FT curves of Ni K-edge EXAFS $k^3\chi(k)$ functions obtained from the XANES spectra and the corresponding fitting curves. (c) *In-situ* Fe K-edge XANES spectra of $NiFeO_x$-B@CNTs. (d) FT curves of Fe K-edge EXAFS $k^3\chi(k)$ functions obtained from the XANES spectra.

To elucidate the real active site for OER in $NiFeO_x$-B@CNTs, we did *in-situ* XAFS measurements with and without applied bias to track the changes in geometric and electronic structures. The XANES of Ni and Fe K-edge spectra of the $NiFeO_x$-B@CNTs electrode were recorded at different applied bias (0 V, 1.3 V, 1.7 V *versus* RHE). As shown in Fig. 5a and insert, with the increasing applied potential, the Ni atoms in $NiFeO_x$-B@CNTs possessed higher valence state as the position of the adsorption edge and white-line peak of Ni K-edge distinctly moved toward the higher energy side. Additionally, the Ni K-edge FT curves (Fig. 5b) clearly depict the average Ni-O bond length shrunk from 1.79 Å to 1.6 Å, implying the oxidation state of Ni atoms is slightly increased [36], which facilitates the formation of the intermediate species (such as OOH*) over the Ni active sites during the OER reaction [37]. In addition, the EXAFS fitting results (Fig. 5b and Table S1 in Supporting information) show that the coordination number of the first shell of Ni-O increases with the applied potential, suggesting the emergence of an oxygen intermediate specie over the Ni active site during the OER reaction. In contrast, the Fe K-edge XANES and FT curves of K-edge EXAFS (Figs. 5c and d) hardly alters under different applied potential, suggesting that the Fe atoms are inert during the OER reaction. These results essentially reveal that the B doping could optimize the Ni 3d $e_g$ orbital of active site, contributing to a highly efficient OER activity.

In summary, a highly efficient and cost-effective $NiFeO_x$-B@CNTs nanoclusters electrocatalyst with highly exposed has been synthesized through a facile pyrolysis strategy. Soft XAS and XPS reveal that the B doping leads to the optimization of 3d electron occupation of the Ni atoms. Accordingly, the as-prepared $NiFeO_x$-B@CNTs hybrids exhibited excellent OER electrocatalytic activity in alkaline solution, with an overpotential as low as 213 mV at 10 mA/cm$^2$ and Tafel slope of 52 mV/dec. Furthermore, *in-situ* XAFS tests indicate that the Ni atoms with increased oxidation are the real active sites. This work shows that the construction of highly

exposed nanoclusters is feasible strategy to create a great deal of novel electrocatalysts for water splitting.

## Declaration of competing interest

The authors declare that they have no known competing financial interests or personal relationships that could have appeared to influence the work reported in this paper.

## Acknowledgments

This work was financially supported by the National Natural Science Foundation of China (Nos. 11975234, 11775225, 12075243 and 12005227). Users with excellence program of Hefei science center CAS, (Nos. 2019HSC-UE002,2020HSC-UE002, 2020HSC-CIP013), the National Key Research and Development Program of China (No. 2021YFA1600800), and the financial support by Postdoctoral Science Foundation of China (Nos. 2019M662202, 2020M682041, 2020TQ0316), and partially carried out at the USTC Center for Micro and Nanoscale Research and Fabrication. The authors would like to thank Beijing Synchrotron Radiation Facility (BSRF), Shanghai Synchrotron Radiation Facility (SSRF) and Beamlines MCD-A and MCD-B (Soochow Beamline for Energy Materials) at NSRL for the synchrotron beamtime.

## Supplementary materials

Supplementary material associated with this article can be found, in the online version, at doi:10.1016/j.cclet.2022.05.038.

## References

[1] R. Gao, D. Yan, Adv. Energy Mater. 10 (2020) 1900954.
[2] B.M. Hunter, H.B. Gray, A.M. Muller, Chem. Rev. 116 (2016) 14120–14136.
[3] I. Katsounaros, S. Cherevko, A.R. Zeradjanin, et al., Angew. Chem. Int. Ed. 53 (2014) 102–121.
[4] B.A. Pinaud, J.D. Benck, L.C. Seitz, et al., Energy Environ. Sci. 6 (2013) 1983–2002.
[5] L. Bai, C.S. Hsu, D.T.L. Alexander, et al., Nat. Energy 6 (2021) 1054–1066.
[6] L. Han, S. Dong, E. Wang, Adv. Mater. 28 (2016) 9266–9291.
[7] F. Song, L. Bai, A. Moysiadou, et al., J. Am. Chem. Soc. 140 (2018) 7748–7759.
[8] M. Carmo, D.L. Fritz, J. Mergel, et al., Int. J. Hydrog. Energy 38 (2013) 4901–4934.
[9] N. Ma, G. Chen, Y. Zhu, et al., Small 16 (2020) 2002089.
[10] B. Li, F. Song, Y. Qian, et al., ACS Appl. Nano Mater. 3 (2020) 9924–9930.
[11] J. Masa, I. Sinev, H. Mistry, et al., Adv. Energy Mater. 7 (2017) 1700381.
[12] G. Li, Y. Tang, T. Fu, et al., Chem. Eng. J. 429 (2022) 132174.
[13] S. Niu, W.J. Jiang, T. Tang, et al., Adv. Funct. Mater. 29 (2019) 1902180.
[14] T. Wang, G. Nam, Y. Jin, et al., Adv. Mater. 30 (2018) 1800757.
[15] H.F. Wang, L. Chen, H. Pang, et al., Chem. Soc. Rev. 49 (2020) 1414–1448.
[16] M.W. Louie, A.T. Bell, J. Am. Chem. Soc. 135 (2013) 12329–12337.
[17] L. Trotochaud, S.L. Young, J.K. Ranney, et al., J. Am. Chem. Soc. 136 (2014) 6744–6753.
[18] J. Zhang, Y. Deng, X. Cai, et al., ACS Catal. 9 (2019) 5998–6005.
[19] M. Peng, C. Dong, R. Gao, et al., ACS Cent. Sci. 7 (2021) 262–273.
[20] Q. Yang, X.P. Fu, C.J. Jia, et al., ACS Catal. 6 (2016) 3072–3082.
[21] D. Das, S. Santra, K.K. Nanda, ACS Appl. Mater. Interfaces 10 (2018) 35025–35038.
[22] Y. Chen, H. Sun, B.C. Gates, Small 17 (2021) 2004665.
[23] S. Yuan, J. Zhang, L. Hu, et al., Angew. Chem. Int. Ed. 60 (2021) 21685–21690.
[24] Y. Zhang, L. Jiao, W. Yang, et al., Angew. Chem. Int. Ed. 60 (2021) 7607–7611.
[25] P. Joshi, H.H. Huang, R. Yadav, et al., Catal. Sci. Technol. 10 (2020) 6599–6610.
[26] D. Wang, Q. Li, C. Han, et al., ACS Cent. Sci. 4 (2018) 112–119.
[27] M. Ramadoss, Y. Chen, Y. Hu, et al., J. Power Source 451 (2020) 227753.
[28] Y. Liang, Y. Li, H. Wang, et al., Nat. Mater. 10 (2011) 780–786.
[29] C. Wang, H. Zhang, J. Wang, et al., Chem. Mater. 29 (2017) 9915–9922.
[30] C. Wang, Z. Guo, W. Shen, et al., Adv. Funct. Mater. 24 (2014) 5511–5521.
[31] K. Chen, Z. Wang, L. Wang, et al., Nano-Micro Lett. 13 (2021) 138.
[32] T.V. Vineesh, M.P. Kumar, C. Takahashi, et al., Adv. Energy Mater. 5 (2015) 1500658.
[33] Y. Li, C. Zhao, ACS Catal. 7 (2017) 2535–2541.
[34] Q. Zhang, T. Li, J. Liang, et al., J. Mater. Chem. A 6 (2018) 7509–7516.
[35] L. Peng, N. Yang, Y. Yang, et al., Angew. Chem. Int. Ed. 60 (2021) 24612–24619.
[36] X. Su, Y. Wang, J. Zhou, et al., J. Am. Chem. Soc. 140 (2018) 11286–11292.
[37] H. Su, W. Zhou, W. Zhou, et al., Nat. Commun. 12 (2021) 6118.